Tuning a magnetic field to generate spinning ferrofluid droplets with controllable speed via nonlinear periodic interfacial waves

Zongxin Yu and Ivan C. Christov

Tuning a magnetic field to generate spinning ferrofluid droplets with controllable speed via nonlinear periodic interfacial waves

Zongxin Yu[*] and Ivan C. Christov[†]

School of Mechanical Engineering, Purdue University, West Lafayette, Indiana 47907, USA

Two dimensional free surface flows in Hele-Shaw configurations are a fertile ground for exploring nonlinear physics. Since Saffman and Taylor's work on linear instability of fluid–fluid interfaces, significant effort has been expended to determining the physics and forcing that set the linear growth rate. However, linear stability does not always imply nonlinear stability. We demonstrate how the combination of a radial and an azimuthal external magnetic field can manipulate the interfacial shape of a linearly unstable ferrofluid droplet in a Hele-Shaw configuration. We show that weakly nonlinear theory can be used to tune the initial unstable growth. Then, nonlinearity arrests the instability, and leads to a permanent deformed droplet shape. Specifically, we show that the deformed droplet can be set into motion with a predictable rotation speed, demonstrating nonlinear traveling waves on the fluid-fluid interface. The most linearly unstable wavenumber and the combined strength of the applied external magnetic fields determine the traveling wave shape, which can be asymmetric.

I. INTRODUCTION

Recently, there has been significant interest in the physics of active and responsive fluids [1, 2]. For example, swimming bacteria can take a suspension of microscopic gears out of equilibrium and extract rectified (useful) work out of an otherwise random system [3]. One promising approach to creating active fluids with controllable properties and behaviors is by suspending many mechanical microswimmers made from shape-programmable materials [4] and actuating them with an external magnetic field [5, 6]. This actuation mechanism is particularly enticing for biological applications due to the safe operation of magnetic fields in the medical setting (for, *e.g.*, targeted therapies and drug delivery *in vivo*) [7]. Even simpler than a suspension of magnetically-responsive mechanical microswimmers is a suspension of ferrofluid droplets, which can also respond to an external magnetic field [8, 9]. Ferrofluids are colloidal dispersion of ferromagnetic nanoparticles in a carrier liquid, such as water, which can be immiscible when placed in another liquid. However, the ferrofluid droplet's interface motion and response to different types of external magnetic fields is not well understood. Previous work has addressed the linear stability of such fluid–fluid interfaces [10, 11], including stationary shapes [12], but not a droplet's nonlinear dynamics or controllable motion. Guided by the well-established ability of nonlinearity to "arrest" long-wave instabilities [13], we demonstrate, using theory and nonlinear simulation, that it is possible to "grow" linearly unstable ferrofluid interfaces into well-defined *permanent* shapes. These permanent shapes, which cannot be further deformed without changing the forcing of the system, can then be considers as *solitary waves*, in the sense

of a "localized wave that propagates along one space direction only, with undeformed shape" [14, p. 11]. Importantly, unlike previous work discussing traveling waves on a ferrofluid interface in a Cartesian configuration [15], we analyze the *fully nonlinear* dynamics of these waves in a novel configuration, and thus ensure they satisfy the solitary wave definition above. Specifically, we show that the resulting coherent droplet shapes are reproducible and controllable via an external magnetic field. These droplets can be set into rotational motion with velocities predictable by the proposed theory, leading to the possibility of an externally-actuated active fluid suspension.

II. GOVERNING EQUATIONS

We study the dynamics of an initially circular ferrofluid droplet (radius R) confined in a Hele-Shaw cell with gap thickness b and surrounded by air (negligible viscosity), as shown in Fig. 1, because "[i]f any [ferro]fluid mechanics problem is likely to be accessible to theory and to direct comparison of theory and experiment it should be this one" [16]. Both fluids are considered incompressible. We propose to apply the radially-varying external magnetic field

$$\mathbf{H} = \underbrace{\frac{I}{2\pi r}\,\hat{\mathbf{e}}_\theta}_{\mathbf{H}_a} + \underbrace{\frac{H_0}{L}r\,\hat{\mathbf{e}}_r}_{\mathbf{H}_r}. \qquad (1)$$

A long wire through the origin, carrying an electric current I, produces the azimuthal component $\mathbf{H}_a$. Anti-Helmholtz coils produce the radial component $\mathbf{H}_r$, where H_0 is a constant and L is a length scale [12, 17]. The combined magnetic field $\mathbf{H} = \mathbf{H}_a + \mathbf{H}_r$ forms an angle with the initially undisturbed interface [18]. The droplet experiences a body force $\propto |\mathbf{M}|\boldsymbol{\nabla}|\mathbf{H}|$, where $\mathbf{M}$ is the magnetization. To study shape dynamics, we assume the ferrofluid is uniformly magnetized, $\mathbf{M} = \chi\mathbf{H}$, where χ is its constant magnetic susceptibility. So, $\boldsymbol{\nabla}|\mathbf{H}| \neq \mathbf{0}$ is the

---

[*] yu754@purdue.edu

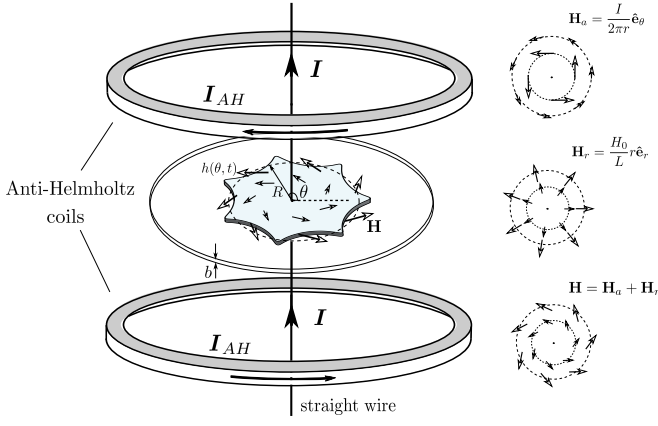[†] Corresponding author.; christov@purdue.edu; http://tmnt-lab.org

FIG. 1. Schematic illustration of a Hele-Shaw cell confining a ferrofluid droplet, initially circular with radius R. The azimuthal magnetic field $\mathbf{H}_a$ is produced by a long wire conveying an electric current I. The radial magnetic field $\mathbf{H}_r$ is produced by a pair of anti-Helmholtz coils with equal currents I_{AH} in opposite directions. The combined external magnetic field $\mathbf{H}$ deforms the droplet, and its interface is given by $h(\theta, t)$. In comparison, the fluid exterior to the droplet (e.g., air) is assumed to have negligible viscosity and velocity.

main contribution to the body force, and the demagnetizing field is negligible, as shown in previous work [17–20].

Enforcing no-slip on the confining boundaries and neglecting inertial terms, the confined flow is governed by a modified Darcy's law [17] with gap-averaged velocity:

$$\mathbf{v} = -\frac{b^2}{12\eta}\boldsymbol{\nabla}\left(p - \Psi\right), \qquad \boldsymbol{\nabla} \cdot \mathbf{v} = 0, \qquad (2)$$

where p is the pressure in the droplet, η is the ferrofluid's viscosity, $\Psi = \mu_0\chi|\mathbf{H}|^2/2$ is a scalar potential accounting for the magnetic body force, and μ_0 is the free-space permeability. Here, $\mathbf{v}$ is the velocity field of the "inner" ferrofluid, while the viscosity of the "outer" fluid is considered negligible (i.e., it is considered inviscid), so the flow exterior to the droplet is neglected. The resulting model is thus, essentially, a one-phase model.

At the boundary of the droplet, the pressure is given by a modified Young–Laplace law [8, 9]:

$$p = \tau\kappa - \frac{\mu_0}{2}(\mathbf{M} \cdot \hat{\mathbf{n}})^2, \qquad (3)$$

where τ is the constant surface tension, and κ is the curvature of the droplet shape. The second term on the right-hand side of Eq. (3) is the magnetic normal traction [8, 9], where $\hat{\mathbf{n}}$ denotes the outward unit normal vector at the interface. This contribution breaks the symmetry of the initial droplet interface, due to the projection of $\mathbf{M}$ onto $\hat{\mathbf{n}}$, and causes the droplet to rotate. The kinematic boundary condition

$$v_n = -\frac{b^2}{12\eta}\boldsymbol{\nabla}\left(p - \Psi\right) \cdot \hat{\mathbf{n}} \qquad (4)$$

requires that the droplet boundary is a material surface.

III. MATHEMATICAL ANALYSIS

We employ the weakly nonlinear approach [21] previously adapted to ferrofluid interfacial dynamics (e.g., [12, 17, 18]). The droplet interface is written as $h(\theta, t) = R + \xi(\theta, t)$, where

$$\xi(\theta, t) = \sum_{k=-\infty}^{+\infty} \xi_k(t)e^{ik\theta} \qquad (5)$$

represents the perturbation of the initially circular interface, with complex Fourier amplitudes $\xi_k(t) \in \mathbb{C}$ and azimuthal wavenumbers $k \in \mathbb{Z}$. The velocity potential $\phi = p - \Psi$ is then expanded into a Fourier series as

$$\phi(r, \theta, t) = \sum_{k\neq 0} \phi_k(t)\left(\frac{r}{R}\right)^{|k|}e^{ik\theta}, \qquad (6)$$

and ϕ_k is expressed in terms of ξ_k through the kinematic boundary condition (4). Substituting Eqs. (5), (6) and (3) into Eq. (2), keeping only terms up to second order in ξ, we find the dimensionless equations of motion ($k \neq 0$):

$$\dot{\xi}_k = \Lambda(k)\xi_k + \sum_{k'\neq 0} F(k, k')\xi_{k'}\xi_{k-k'} + G(k, k')\dot{\xi}_{k'}\xi_{k-k'}. \qquad (7)$$

The mode-coupling functions in Eq. (7) are given by

$$F(k, k') = \frac{|k|}{R}\left\{\frac{\mathrm{N_{Ba}}}{R^4}[3 - \chi k'(k - k')]\right.$$
$$+ \mathrm{N_{Br}}\{1 + \chi[k'(k - k') + 1]\}$$
$$\left. - \frac{1}{R^3}\left[1 - \frac{k'}{2}(3k' + k)\right] + \frac{2\chi\sqrt{\mathrm{N_{Ba}N_{Br}}}}{R^2}ik'\right\}, \qquad (8a)$$

$$G(k, k') = \frac{1}{R}[(\mathrm{sgn}(kk') - 1)|k| - 1], \qquad (8b)$$

where $\mathrm{sgn}(x) = x/|x|$ for $x \neq 0$ and $\mathrm{sgn}(0) = 0$.

From mass conservation, $\xi_0 = -\sum_{k>0}|\xi_k|^2/R \ \forall t \geq 0$. Here,

$$\Lambda(k) = \underbrace{\frac{|k|}{R^3}(1 - k^2)}_{\text{surface tension}} - \frac{2\mathrm{N_{Ba}}}{R^4}|k| + 2(1 + \chi)\mathrm{N_{Br}}|k|$$
$$- \frac{2\chi\sqrt{\mathrm{N_{Ba}N_{Br}}}}{R^2}ik|k| \qquad (9)$$

denotes the (complex) linear growth rate, and

$$\mathrm{N_{Ba}} = \frac{\mu_0\chi I^2}{8\pi^2\tau L}, \qquad \mathrm{N_{Br}} = \frac{\mu_0\chi H_0^2 L}{2\tau} \qquad (10)$$

are the magnetic Bond numbers quantifying the ratio of azimuthal and radial magnetic forces to the capillary force, respectively. Terms multiplied by χ arise from the magnetic normal stress. The time and length scales used in the nondimensionalization are $12\eta L^3/\tau b^2$ and L, respectively.

IV. LINEAR REGIME

First, consider Eq. (7), neglecting quadratic terms in ξ_k, then $\Re[\Lambda(k)] = \lambda(k)$ governs the exponential growth or decay of infinitesimal perturbations. For $\lambda(k) > 0$, the interface is unstable. Specifically, Eq. (9) indicates that the radial magnetic field term $\propto (1 + \chi)N_{Br}$ is destabilizing, while the azimuthal term $\propto N_{Ba}$ and surface tension are stabilizing. The most unstable mode k_m solves $d\lambda(k)/dk = 0$:

$$k_m = \sqrt{\frac{1}{3}\left[1 - \frac{2N_{Ba}}{R} + 2(1+\chi)N_{Br}R^3\right]}. \qquad (11)$$

This wavenumber characterizes the dominant $\lfloor k_m \rfloor$-fold symmetry of a pattern. Note that the normal stress from the azimuthal magnetic field does not contribute to the linear dynamics.

The phase velocity of each mode,

$$v_p = -\Im[\Lambda(k)]/k = 2\chi\sqrt{N_{Ba}N_{Br}}k/R^2 \qquad (12)$$

in the linear regime, is set by $\Im[\Lambda(k)]$. A periodic shape on $[0, 2\pi]$ forms a closed curve, meaning wave propagation is manifested as rotation of the droplet. Motion is caused by the magnetic normal stresses arising from the combined magnetic field. Intuitively, from vector projection, we observe that only the combined azimuthal and radial magnetic field can break the symmetry and cause a force imbalance leading to motion. This linear analysis indicates that perturbations of the droplet interface can propagate (and, since $v_p = v_p(k)$, they also experience dispersion). Such wavepackets will either decay or blow-up exponentially according to the sign of $\lambda(k)$. However, this is not the whole story, and *nonlinearly stable* traveling shapes exist, as we now show.

V. NONLINEAR REGIME

To demonstrate the possibility of nonlinear traveling waves in this system, we numerically solve the weakly nonlinear mode-coupling equations (7) for five modes (*i.e.*, $k, 2k, \ldots, 5k$). The fundamental mode $k = 7$ is chosen to allow propagating solutions over a wider swath of the (N_{Ba}, N_{Br}, k_m) space (compared to choosing $k < 7$), while only requiring modest spatial resolution for simulations (compared to $k > 7$). We verified that the amplitudes $|c_n|$ and phases $\angle[c_n]$ of modes saturate at late times, leading to permanent propagating profiles with $\xi_{nk}(t) = c_n e^{in\omega(k)t}$ (see below).

Next, we perform fully nonlinear simulations to validate the weakly nonlinear predictions. The vortex sheet method is a standard sharp-interface technique for simulating dynamics of Hele-Shaw flows [22]. It is based on a boundary integral formulation in which the interface is formally replaced by a generalized vortex sheet [23] with a distribution of vortex strengths $\gamma(s, t)$, where s is the

arclength coordinate. We adapt this approach to handle ferrofluids under imposed magnetic fields. First, we express the velocity of the interface solely in terms of the interface position. To do so, it is convenient to identify the position vector in $\mathbb{R}^2$ with a scalar $z(s, t) \in \mathbb{C}$ (* denotes complex conjugate) [23–25]. Second, to advance the interface, we solve the dimensionless equations

$$z_t^* = -\frac{\gamma}{2z_s} + \frac{1}{2\pi i}\mathcal{P}\oint \frac{\gamma(s', t)}{z(s, t) - z(s', t)}ds', \qquad (13a)$$

$$\frac{\gamma}{2} = \Re\left\{\frac{z_s}{2\pi i}\mathcal{P}\oint \frac{\gamma(s', t)}{z(s, t) - z(s', t)}ds'\right\}$$
$$+ \left[\kappa(s, t) - (\mathbf{M}\cdot\hat{\mathbf{n}})^2 - \Psi\right]_s, \qquad (13b)$$

iteratively for the velocity z_t, where $(\cdot)_t \equiv \partial(\cdot)/\partial t$, $(\cdot)_s \equiv \partial(\cdot)/\partial s$, $i = \sqrt{-1}$, and $\mathcal{P}$ represents principal value integration. Here, $\Psi = N_{Ba}r^{-2} + N_{Br}r^2$, and $(\mathbf{M}\cdot\hat{\mathbf{n}})^2 = \chi\left[\sqrt{N_{Ba}}r^{-1}(\hat{\mathbf{e}}_\theta\cdot\hat{\mathbf{n}}) + \sqrt{N_{Br}}r(\hat{\mathbf{e}}_r\cdot\hat{\mathbf{n}})\right]^2$ is the dimensionless magnetic normal stress. Time advancement is accomplished by the Crank–Nicolson scheme. The spatial discretization is implemented on an array of Lagrangian points ($N = 1024$) with uniform Δs; see Appendix B for further details, including algorithm flowchart and grid convergence study.

VI. EVOLUTIONARY DYNAMICS

The evolution of perturbed harmonic modes ξ_k under the fully nonlinear simulation and the weakly nonlinear approximation are shown in Fig. 2(a). Starting from small initial values ($\xi_k|_{k=7} = 0.002$, $\xi_{nk} = 0$ for $n > 1$) with N_{Ba}, N_{Br}, R, χ set so that the most unstable mode is equal to the fundamental mode ($k_m = k = 7$), they saturate at late times. The perturbed circular interface grows exponentially in the linear regime and then matches the weakly nonlinear approximation at intermediate times ($t \in [0, t_w]$). The nonlinear simulations take longer to saturate ($t \in [t_w, t_e]$) and do so at higher final amplitudes compared to the weakly nonlinear result. The time-domain evolution is also shown in Fig. 2(b), evolving from a nearly flat (unwound circular) interface into a permanent propagating profile [26].

The rotating droplet, shown in Fig. 2(c), has a polygonal shape with the symmetry set by the fundamental mode, $k = 7$. The fully nonlinear profile has a sharper peak compared to the weakly nonlinear approximation, which is otherwise in good agreement. The key discovery of the present work is the *stable rotating shape*, which we now seek to analyze as a nonlinear wave phenomenon [14].

VII. WHEN DOES WEAKLY NONLINEAR STABILITY IMPLY NONLINEAR STABILITY?

A deficiency of linear and weakly nonlinear analyses is that they do *not* provide sufficient conditions for stability.
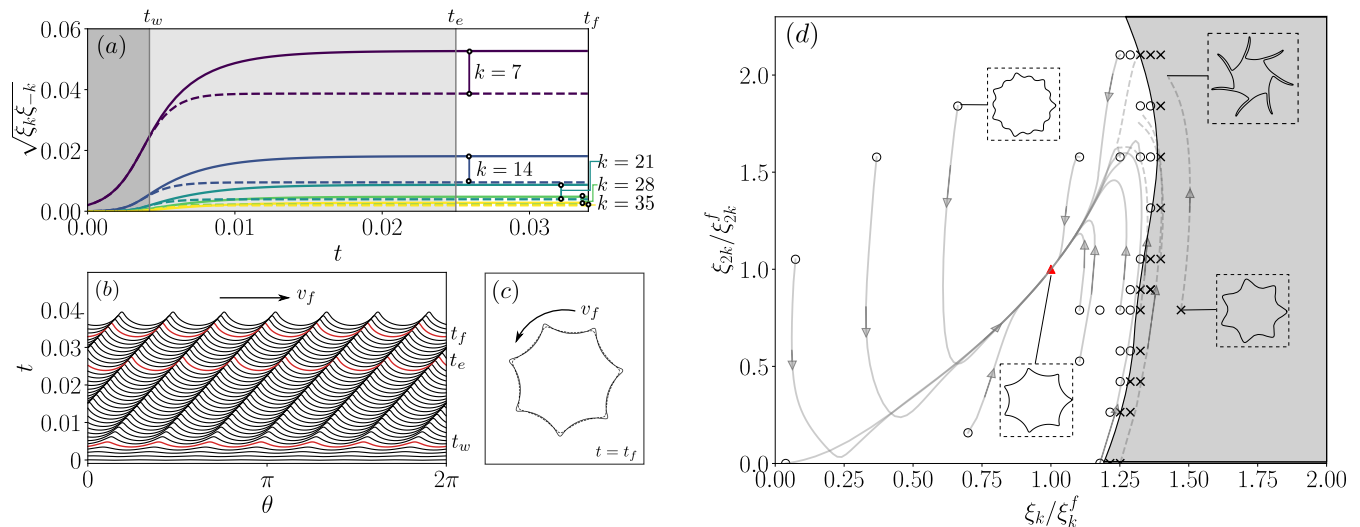
FIG. 2. (a) The evolution of the first 5 harmonic modes from fully nonlinear simulation (solid) and weakly nonlinear approximation (dashed), for $N_{Ba} = 1.0$, $N_{Br} = 37$, $R = 1$, and $\chi = 1$ (same parameters for (b), (c) and (d)). (b) The fully nonlinear evolution of the interface from a small perturbation of the flat base state into a permanent traveling wave (rotating droplet). (c) Comparison between the final shape from fully nonlinear simulation (solid) and weakly nonlinear approximation (dashed); (d) Stability diagram based on the first two harmonic modes of the final shape (marked with ▲) shown in (b); ○ (resp. ×) denotes the stable (resp. unstable) initial conditions, solid (resp. dashed) curves tract the stable (resp. unstable) evolution trajectories. The unstable region is shaded, and the 'f' superscript represents the final harmonic mode amplitude.

Linearly stable base states can be nonlinearly unstable [27], and *vice versa*. Importantly, however, our nonlinear traveling wave solution is a local *attractor* (following the terminology from [28]); see Fig. 2(d).

Shapes in a neighborhood of the propagating profile, subject to small ($\xi_{k,2k}/\xi_{k,2k}^f \ll 1$) or intermediate ($\xi_{k,2k}/\xi_{k,2k}^f = \mathcal{O}(1)$) initial perturbations, converge to it. Larger perturbations (shaded region) lead to *nonlinear instability* of the weakly nonlinearly stable profiles; "fingers" continue to rotate and grow without bound under the effect of the radial magnetic field $\propto N_{Br}$, which increases with distance to the center of the droplet. Convergence to the attractor is sensitive to the initial amplitude of the first harmonic mode ξ_k. For the chosen parameters, $\lambda(k) > 0$ and $\lambda(2k) < 0$: high wavenumbers decay and the fundamental wavenumber grow in the linear stage. Consequently, for low ξ_k/ξ_k^f and high ξ_{2k}/ξ_{2k}^f, the low wavenumber modes grow and saturate, as high wavenumber modes decay exponentially in the linear regime. With higher initial ξ_k/ξ_k^f, the perturbed droplet will not go through the linear regime, and the amplitudes of both modes will rapidly increase to create a skewed shape, with multivalued $h(\theta, t)$, for which harmonic modes can no longer be defined. Note that Fig. 2(d) is a projection in the (ξ_k, ξ_{2k}) plane, where the initial values of $\xi_{3k}, \xi_{4k}, \xi_{5k}$ are set as the final amplitudes (and phases) from the weakly nonlinear equations. A fast Fourier transform was used to decompose the nonlinear profile into normal modes that we plot in this figure. Note that even though Fig. 2(a) indicates ξ_{3k} makes a

non-trivial contribution to the final shape, while ξ_{4k}, ξ_{5k} play a smaller role, the projection is sufficient to conclude that the propagating wave profile is an attractor.

VIII. PROPAGATION VELOCITY

A permanent traveling wave profile has $\xi(\theta, t) = \Xi(k\theta - \omega t)$, and $v_f = \omega/k$ is its propagation velocity. Expressing the modes' complex amplitudes as $\xi_{nk}(t) = c_n e^{-in\omega(k)t}$, with constant $c_n \in \mathbb{C}$ that account for their relative phases, we have $v_p(k, t) = n\omega(k)/nk = v_f$. The mean v_p of the first five harmonics is used to calculate v_f^F for the fully nonlinear simulation and also v_f^W for the weakly nonlinear approximation. Meanwhile, $v_f^L = v_p$ as given by Eq. (12).

For a quantitative comparison, three sets of parameters are considered, fixing $\chi = 1$. Two sets (i) and (ii) are for $k_m = 7$, and the variation of N_{Br} is according to Eq. (11). A third set (iii) explores the effect of k_m under the same linear propagation velocity v_f^L. Figure 3(a) compares the final propagating velocity predictions. Both v_f^L and v_f^W are in relatively good agreement with v_f^F for small velocities. When $N_{Ba} \to 0$ (the magnetic field becomes radial), only a stationary (non-rotating) droplet ($v_f = 0$) exists [12]. For higher v_f, the larger deviation in the predictions highlights the importance of nonlinearity. Nevertheless, the linear and weakly nonlinear results follow a similar trend. Importantly, v_f^L and v_f^W help identify the key control factors: the coupled magnetic field strength $\sqrt{N_{Ba}N_{Br}}$ and the radius of the initial droplet R. The
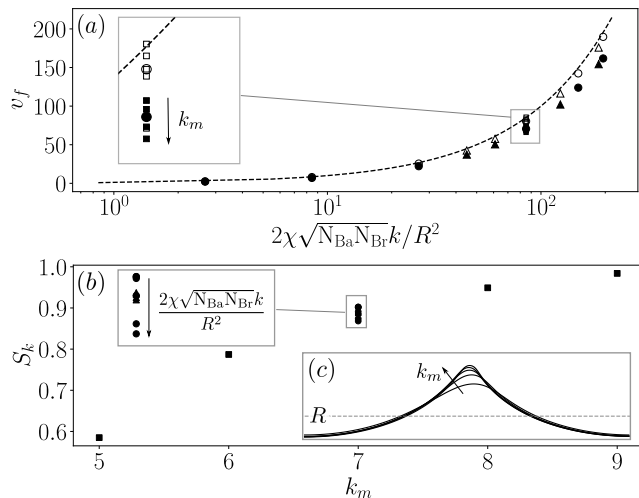
FIG. 3. (a) Comparison of the propagation velocity predicted by linear theory v_f^L (dashed), weakly nonlinear theory v_f^W (empty symbols), and fully nonlinear simulation v_f^F (filled symbols). The circles represent results for case (i) $R = 1$ fixed and $N_{Ba} \in [0, 10^{-3}, 10^{-2}, 10^{-1}, 1, 3, 5]$, the triangles represent results for case (ii) $N_{Br} = 1$ fixed with N_{Br} varying according to $R \in [0.8, 0.9, 1.1, 1.2]$, and the squares represent case (iii) $k_m \in [5, 6, 7, 8, 9]$, $R = 1$ and N_{Ba}, N_{Br} determined so that $v_f^L = 85.16$. (b) The skewness Sk of the fully nonlinear profile. (c) The permanent wave shape (only one wavelength shown).

salient physics uncovered is that the propagating velocity can be non-invasively tuned.

IX. TRAVELING WAVE SHAPE

The most unstable mode k_m sets the propagating profile, which has a sharper peak for higher k_m [Fig. 3(c)]. To quantify the shape change, we introduce the skewness $Sk(t) = \langle \xi^3 \rangle / \langle \xi^2 \rangle^{3/2}$, which is used to define the vertical asymmetry of nonlinear surface water waves [29, 30]; $Sk > 0$ corresponds to narrow crests and flat troughs. Here, $\langle \cdot \rangle = \frac{1}{2}\pi \int_0^{2\pi} (\cdot) \, d\theta$. Figure 3(b) shows that Sk (for the fully nonlinear propagation) increases with k_m, as expected from the sharper peaks in Fig. 3(c). This observation also explains why v_f^L becomes a worse approximation of v_f^F as k_m increases [inset of Fig. 3(a)]: smoother peaks (lower k_m) are better captured by the linear theory based on harmonic modes.

Figure 3(c) reveals that the wave profile for $k_m = 5$ ($N_{Ba} = 1.9$, $N_{Br} = 19.5$) is more asymmetric than the one for $k_m = 9$ ($N_{Ba} = 0.60$, $N_{Br} = 60.8$). Under a purely radial magnetic field ($N_{Ba} = 0$), the stationary shape has azimuthal symmetry [12]. For the combined magnetic field, on the other hand, the dimensionless governing Eq. (2) and pressure boundary condition in Eq. (3)

can be rewritten as

$$\mathbf{v} = -\boldsymbol{\nabla}\left(p - N_{Ba}\frac{1}{r^2} - N_{Br}r^2\right), \quad (14)$$

$$p = \kappa - \left[\chi\frac{N_{Ba}}{r^2}(\hat{\mathbf{e}}_\theta \cdot \hat{\mathbf{n}})^2 + \chi N_{Br}r^2(\hat{\mathbf{e}}_r \cdot \hat{\mathbf{n}})^2 \right.$$
$$\left. + 2\chi\sqrt{N_{Ba}N_{Br}}(\hat{\mathbf{e}}_\theta \cdot \hat{\mathbf{n}})(\hat{\mathbf{e}}_r \cdot \hat{\mathbf{n}})\right], \quad (15)$$

where $\hat{\mathbf{e}}_\theta \cdot \hat{\mathbf{n}} = -h_\theta/(h^2 + h_\theta^2)$, $\hat{\mathbf{e}}_r \cdot \hat{\mathbf{n}} = h/(h^2 + h_\theta^2)$, and $h_\theta = \partial h/\partial \theta$. The magnetic scalar potential in Eq. (14) results from the body force, and the terms premultiplied by χ in Eq. (15) represent the magnetic normal stress. For a droplet with symmetric azimuthal perturbation, the body force alone cannot break the symmetry. Therefore, the asymmetry of shapes discussed is to be attributed to the magnetic normal stress.

This observation can be intuitively understood by considering one wavelength of a symmetric waveform. The first three terms on the right-hand side of Eq. (15) are equal on both sides of the peak, while the fourth term changes at the peak due to the sign of h_θ, which requires different curvatures on either side of the peak to remain balanced. Therefore, $\sqrt{N_{Ba}N_{Br}}$ can be taken as the measure of the coupling effect between the magnetic field components.

To further understand the asymmetry of propagating shapes induced by the combined magnetic field, we extend the parameters of case (i) to a new case (iv): $k_m = 7$, $R = 1$ and N_{Br} varying according to N_{Ba} (see Fig. 4 caption). To quantify the fore-aft asymmetry of the shape, we introduce $As(t) = \langle \mathcal{H}[\xi]^3 \rangle / \langle \xi^2 \rangle^{3/2}$ [29, 30]; $\mathcal{H}[\cdot]$ is the Hilbert transform. For $As > 0$, waves tilt "forward" (i.e., counter-clockwise).

Figure 4(a) shows $As(t)$ for different $\sqrt{N_{Ba}N_{Br}}$, which quantifies the coupled field effect, starting with small symmetric perturbations. For a stable case, $As(t)$ reaches a maximum value ($t \approx t_1$) during the initial unstable weakly nonlinear growth (dark shadow region), and asymptotes to a value close to zero ($t \geq t_6$). The differences in the final propagating profile (under the same k_m) shown in Fig. 4(b) are hard to capture, which is consistent with the observation in Fig. 3(b). For the unstable cases, "wave breaking" occurs, which is highlighted by a change of sign of As. Also, now, $As(t)$ no longer saturates at late t. Instead $As(t)$ crosses zero (at $t \gtrsim t_3$) and approaches a singularity. This unstable example is shown in the second row of Fig. 4(c). As its amplitude first grows, the wave tilts forward ($t = t_2$), but nonlinear effects restore its symmetry ($t = t_3$). Subsequently, the wave tilts backwards ($t = t_4, t_5$) and its amplitude continues to grow ($t = t_6$). The calculation of As then fails because $\mathcal{H}$ requires the perturbation $\xi(\theta, t)$ to be single-valued in θ. The distorted wave has a wider base and evolves into long unstable fingers.

Note that N_{Ba}/N_{Br} also increases with $\sqrt{N_{Ba}N_{Br}}$ for our choices of N_{Ba} and N_{Br}. Equation (9) shows that the radial magnetic field is destabilizing, while surface
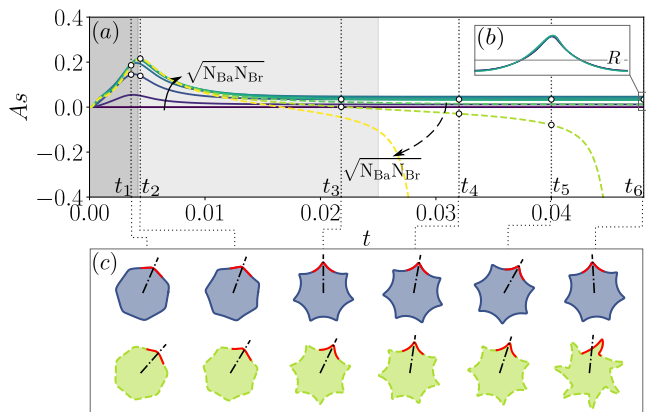
FIG. 4. (a) Time evolution of the wave profile asymmetry for different combination of $N_{Ba} \in [0, 0.1, 1, 3, 5, 6, 7, 8, 9]$ and N_{Br} varying so that $k_m = 7$ for $R = 1$. Solid curves represent stable cases yielding a propagating profile; dashed curves represent unstable cases in which the profile distorts and grows without bound. (b) Permanent wave profiles that emerge and propagating in a stable manner. (c) Stable (top, with $N_{Ba} = 1, N_{Br} = 37$) and unstable (bottom, $N_{Ba} = 8, N_{Br} = 41$) evolution of the profile. The instants of time (at which the shapes in (c) are shown) are marked with white dots in (a), superimposed on the asymmetry profiles.

tension ($k > 2$ here) and the azimuthal field are stabilizing. However, the nonlinear simulations indicate that, for the same k_m, increasing N_{Ba}/N_{Br} can induce instability because it engenders a larger v_f (and As), leading to a global bifurcation with Fig. 2(d) as one stable slice. This result has an analogy to solitary waves in equations of the Kortweg–de Vries (KdV) type. Specifically, initial perturbations grow, deforming a shape until nonlinearity is balanced by dispersion, when a permanent wave emerges [31]. However, depending on the form of the nonlinearity, not all such permanent waves are stable attractors, and conditions must be placed on the wave speed [32].

X. CONCLUSION

This study demonstrates how a perturbed circular ferrofluid droplet can evolve into a nonlinearly stable rotating shape. The most unstable mode sets how perturbations evolve into a permanent profile (and its skewness and asymmetry). Weakly nonlinear theory, in hand with fully nonlinear simulations, revealed permanent rotating shapes (traveling waves) with predictable propagation velocity. We showed how the coupling of the magnetic field

components modifies the asymmetry and the nonlinear instability.

Although the manipulation of the linear growth rate of interfacial perturbations in Hele-Shaw cells is well studied [33], including extensions based on the weakly nonlinear expansion from Eq. (7) [34], the *control* of the dynamic, *fully nonlinear*, patterns is not. Our approach harnesses the magnitude and the direction of coupled magnetic fields to generate ferrofluid droplets, with well-characterized shapes and rotational speeds, by purely *external* means.

Open questions remain: *e.g.*, which fundamental modes evolve into propagating shapes? Work on the stationary problem [17, 35] gives a hint, however, for a propagating shape the Birkhoff integral equation [36] must be solved, making an extension of [17, 35] challenging. Interestingly, our simulations also reveal that patterns predicted as stable by weakly nonlinear analysis can be unstable. In Appendix A, we provide an example showing that perturbations with $k = 4$ will not evolve into either a stationary or a propagating shape (although both are predicted to exist by weakly nonlinear analysis).

Additionally, does this system accommodate more than one propagating wave? If so, do such waves keep their shapes upon collision, as with soliton interactions [31, 37]? Previous studies derived KdV equations for unidirectional small-amplitude, long-wavelength disturbances on fluid–fluid interfaces in Hele-Shaw [38] and axisymmetric ferrofluid configurations [19, 39], demonstrating the celebrated "sech^2" solitary wave. Instead, in our study without such restrictions, we discovered *periodic* traveling nonlinear waves, which are akin to the *cnoidal* solutions of periodic KdV, *i.e.*, the fundamental nonlinear modes ("soliton basis states") [40]. Additionally, we observed wave breaking [Fig. 4(c,bottom)].

Finally, it would be of interest to verify the proposed shape manipulation strategies by laboratory experiments. Previous theoretical studies [17, 41–43] suggest that many exact stationary droplet shapes are unstable, thus their relevance to experimental studies is limited. On the other hand, the nonlinear simulations in our study, showing stable rotation, pave the way for future experimental realizations.

ACKNOWLEDGMENTS

[1] M. C. Marchetti, J. F. Joanny, S. Ramaswamy, T. B. Liverpool, J. Prost, M. Rao, and R. A. Simha, Hydrodynamics of soft active matter, Rev. Mod. Phys. **85**, 1143 (2013).

[2] D. Saintillan, Rheology of Active Fluids, Annu. Rev. Fluid Mech. **50**, 563 (2018).

[3] A. Sokolov, M. M. Apodaca, B. A. Grzybowski, and I. S. Aranson, Swimming bacteria power microscopic gears, Proc. Natl Acad. Sci. USA **107**, 969 (2010).

[4] G. Z. Lum, Z. Ye, X. Dong, H. Marvi, O. Erin, W. Hu, and M. Sitti, Shape-programmable magnetic soft matter, Proc. Natl Acad. Sci. USA **113**, E6007 (2016).

[5] T. Xu, J. Zhang, M. Salehizadeh, O. Onaizah, and E. Diller, Millimeter-scale flexible robots with programmable three-dimensional magnetization and motions, Science Robotics **4**, eaav4494 (2019).

[6] J. Giltinan, P. Katsamba, W. Wang, E. Lauga, and M. Sitti, Selectively controlled magnetic microrobots with opposing helices, Appl. Phys. Lett. **116**, 134101 (2020).

[7] B. J. Nelson, I. K. Kaliakatsos, and J. J. Abbott, Microrobots for Minimally Invasive Medicine, Annu. Rev. Biomed. Eng. **12**, 55 (2010).

[8] R. Rosensweig, *Ferrohydrodynamics* (Dover Publications, Mineola, NY, 2014) republication of the 1997 edition.

[9] E. Blums, A. Cebers, and M. Maiorov, *Magnetic Fluids* (De Gruyter, Berlin, 1997).

[10] R. E. Rosensweig, M. Zahn, and R. Shumovich, Labyrinthine instability in magnetic and dielectric fluids, J. Magn. Magn. Mater. **39**, 127 (1983).

[11] D. P. Jackson, R. E. Goldstein, and A. O. Cebers, Hydrodynamics of fingering instabilities in dipolar fluids, Phys. Rev. E **50**, 298 (1994).

[12] P. H. A. Anjos, S. A. Lira, and J. A. Miranda, Fingering patterns in magnetic fluids: Perturbative solutions and the stability of exact stationary shapes, Phys. Rev. Fluids **3**, 044002 (2018).

[13] A. L. Bertozzi and M. C. Pugh, Long-wave instabilities and saturation in thin film equations, Comm. Pure Appl. Math. **51**, 625 (1998).

[14] M. Remoissenet, *Waves Called Solitons: Concepts and Experiments*, Advanced Texts in Physics (Springer, Berlin/Heidelberg, 1999).

[15] S. A. Lira and J. A. Miranda, Nonlinear traveling waves in confined ferrofluids, Phys. Rev. E **86**, 056301 (2012).

[16] D. Bensimon, L. P. Kadanoff, S. Liang, B. I. Shraiman, and C. Tang, Viscous flows in two dimensions, Rev. Mod. Phys. **58**, 977 (1986).

[17] S. A. Lira and J. A. Miranda, Ferrofluid patterns in Hele-Shaw cells: Exact, stable, stationary shape solutions, Phys. Rev. E **93**, 013129 (2016).

[18] J. A. Miranda and R. M. Oliveira, Time-dependent gap Hele-Shaw cell with a ferrofluid: Evidence for an interfacial singularity inhibition by a magnetic field, Phys. Rev. E **69**, 066312 (2004).

[19] D. Rannacher and A. Engel, Cylindrical Kortewegde Vries solitons on a ferrofluid surface, New. J. Phys. **8**, 108 (2006).

[20] P. H. A. Anjos, G. D. Carvalho, S. A. Lira, and J. A. Miranda, Wrinkling and folding patterns in a confined ferrofluid droplet with an elastic interface, Phys. Rev. E **99**, 022608 (2019).

[21] J. A. Miranda and M. Widom, Radial fingering in a Hele-Shaw cell: a weakly nonlinear analysis, Physica D **120**, 315 (1998).

[22] A. J. Roberts, A stable and accurate numerical method to calculate the motion of a sharp interface between fluids, IMA J. Appl. Math. **31**, 13 (1983).

[23] A. Prosperetti, Boundary Integral Methods, in *Drop-Surface Interactions*, CISM International Centre for Mechanical Sciences, Vol. 456, edited by M. Rein (Springer-Verlag, Wien, 2002) pp. 219–235.

[24] M. J. Shelley, A study of singularity formation in vortex-sheet motion by a spectrally accurate vortex method, J. Fluid Mech. **244**, 493 (1992).

[25] M. J. Shelley, F.-R. Tian, and K. Wlodarski, Hele-Shaw flow and pattern formation in a time-dependent gap, Nonlinearity **10**, 1471 (1997).

[26] See Supplemental Material at [URL will be inserted by publisher] for a video of this process.

[27] P. G. Kevrekidis, D. E. Pelinovsky, and A. Saxena, When Linear Stability Does Not Exclude Nonlinear Instability, Phys. Rev. Lett. **114**, 214101 (2015).

[28] S. Li, J. S. Lowengrub, J. Fontana, and P. Palffy-Muhoray, Control of Viscous Fingering Patterns in a Radial Hele-Shaw Cell, Phys. Rev. Lett. **102**, 174501 (2009).

[29] A. B. Kennedy, Q. Chen, J. T. Kirby, and R. A. Dalrymple, Boussinesq modeling of wave transformation, breaking, and runup. I: 1D, J. Waterw. Port. Coast. **126**, 39 (2000).

[30] T. J. Maccarone, The biphase explained: understanding the asymmetries in coupled Fourier components of astronomical time series, Mon. Not. R. Astron. Soc. **435**, 3547 (2013).

[31] N. J. Zabusky and M. D. Kruskal, Interaction of "Solitons" in a Collisionless Plasma and the Recurrence of Initial States, Phys. Rev. Lett. **15**, 240 (1965).

[32] J. L. Bona, P. E. Souganidis, and W. A. Strauss, Stability and instability of solitary waves of Korteweg-de Vries type, Proc. R. Soc. Lond. A **411**, 395 (1987).

[33] L. C. Morrow, T. J. Moroney, and S. W. McCue, Numerical investigation of controlling interfacial instabilities in non-standard Hele-Shaw configurations, J. Fluid Mech. **877**, 1063 (2019).

[34] E. O. Dias and J. A. Miranda, Control of radial fingering patterns: A weakly nonlinear approach, Phys. Rev. E **81**, 016312 (2010).

[35] E. S. G. Leandro, R. M. Oliveira, and J. A. Miranda, Geometric approach to stationary shapes in rotating Hele-Shaw flows, Physica D **237**, 652 (2008).

[36] G. Birkhoff, *Taylor instability and laminar mixing*, Tech. Rep. LA-1862 (Los Alamos Scientific Laboratory, 1954).

[37] T. Soomere, Solitons Interactions, in *Encyclopedia of Complexity and Systems Science*, edited by R. A. Meyers (Springer, New York, NY, 2009) pp. 8479–8504.

[38] M. Zeybek and Y. C. Yortsos, Long waves in parallel flow in Hele-Shaw cells, Phys. Rev. Lett. **67**, 1430 (1991).

[39] E. Bourdin, J.-C. Bacri, and E. Falcon, Observation of Axisymmetric Solitary Waves on the Surface of a Ferrofluid, Phys. Rev. Lett. **104**, 094502 (2010).

[40] A. R. Osborne, E. Segre, G. Boffetta, and L. Cavaleri, Soliton basis states in shallow-water ocean surface waves, Phys. Rev. Lett. **67**, 592 (1991).

[41] S. A. Lira, J. A. Miranda, and R. M. Oliveira, Stationary shapes of confined rotating magnetic liquid droplets, Phys. Rev. E **82**, 036318 (2010).

[42] E. O. Dias, S. A. Lira, and J. A. Miranda, Interfacial patterns in magnetorheological fluids: Azimuthal field-induced structures, Phys. Rev. E **92**, 023003 (2015).

[43] E. Álvarez-Lacalle, J. Ortín, and J. Casademunt, Nonlinear Saffman-Taylor instability, Phys. Rev. Lett. **92**, 054501 (2004).

Appendix A: Unstable pattern with $k = 4$

As mentioned in the main text, linear (or even weakly nonlinear) stability does not always imply nonlinear stability (see also [27]). Indeed, it is not known under what conditions the weakly-nonlinear stable droplet shapes are actually nonlinearly stable. In the main text, we presented examples for which this implication holds true. Here, in Fig. 5, we demonstrate, for completeness, an example to the contrary. To the best of our knowledge, such an example has not been analyzed before, and thus remains an avenue of future work. This exploration also requires caution, to rule out physical from numerical instability.
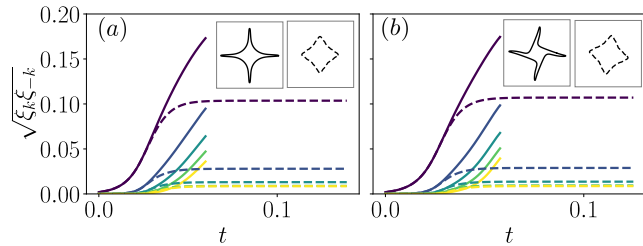

FIG. 5. The unstable evolution of the first 5 harmonic modes ($k = 4, 8, 12, 16, 20$) from fully nonlinear simulation (solid) and their stable evolution from weakly nonlinear approximation (dashed) for (a) nonrotating ($k_m = 4$, $N_{Ba} = 0$) and (b) rotating ($k_m = 4$, $N_{Ba} = 1$) shapes.

Appendix B: Implementation of the numerical method and grid convergence

The principal value integration in Eqs. (13) is performed numerically by a spectrally accurate spatial scheme [24]:

$$PV_j = \frac{2\Delta s}{2\pi i} \sum_{j+k \text{ odd}} \frac{\gamma_k}{z_j - z_k}, \tag{B1}$$

where a j subscript denotes the evaluation of a quantity at the jth Lagrangian grid point $j\Delta s$ with $\Delta s = L/N$, $L = \oint ds$, and N is the number of grid points. The parametrization of the interface via its arclength reduces the stiffness of the numerical problem caused by the presence of third-order spatial derivatives. A rearrangement of the grid points is conducted with cubic interpolation, after each time step, to maintain uniform grid spacing Δs. The uniform arclength spacing then allows the use of the second-order central differentiation formulæ for all derivatives. A fixed-point iteration scheme is used to resolve the implicit Eq. (13b) to obtain γ_j at each interface point z_j, as shown schematically in Fig. 6.

Time advancement (superscripts denote the time step number) is accomplished with a Crank–Nicolson scheme:

$$z^{*n+1} = z^{*n} - \frac{\Delta t}{2}\left[\frac{\gamma^{n+1}}{2z_s^{n+1}} + \frac{\gamma^n}{2z_s^n}\right] + \frac{\Delta t}{2}\left[PV^{n+1} + PV^n\right], \tag{B2}$$

where both of the nonlinear terms $\gamma^{n+1}/2z_s^{n+1}$ and PV^{n+1} are obtained by subiteration with index m, as shown schematically in Fig. 6. Equation (B2) converges and $z^{n+1} = z^{m+1}$ when $\|z^{m+1} - z^m\| < \text{tol}_z$ with $\text{tol}_z = 0.1 \max |z_t^n|\Delta t$.

A grid convergence study with 4 levels of the grid resolution was conducted for two cases: $k_m = 7$ and $k_m = 9$ with $N_{Ba} = 1$. The most frequently used case in the main text is $k_m = 7$, while the sharper peaks for $k_m = 9$ demand on the highest grid resolution. Figure 7(a) shows the spectral energy content of harmonic modes (k, $2k$, $3k$, ...) of the propagating waveform, where the "piling up" near the tail on the finest grid ($N = 2048$) is numerical noise. This plot supports our decision to consider the $N = 1024$ grid as offering sufficient resolution. Figure 7(b) shows the root-mean-squared error in the shape z itself, taking $\hat{z}$ as the "reference shape" on the $N = 2048$ grid. The error decreases with grid refinement. The error at $N = 256$ for $k_m = 9$ is not shown for the propagating shape because the scheme is not even stable on such a coarse mesh for this case.

Figure 7 further shows the evolution of (c) the skewness Sk and (d) the asymmetry As. The skewness matches well on all grids used, showing it is a well-converged quantity, while the asymmetry is seen to be more sensitive to the grid resolution. The differences between $N = 1024$ and $N = 2048$ are small enough so that it is safe to use $N = 1024$ for the simulations reported in the main text, considering the significantly higher computational cost incurred by using finer grids.

$$z^n(x+iy)$$

$$z^{m=0} = z^n, \gamma^{l=0} = \gamma^n$$

$$PV^{l+1} = \frac{1}{2\pi i} \mathcal{P} \oint \frac{\gamma^l(s',t)}{z^m(s,t) - z^m(s',t)} ds'$$

$$\frac{\gamma^{l+1}}{2} = \Re\left\{ z_s^m PV^{l+1} \right\} + C(z^m)$$

$$l = l+1$$

solve Eq. (13b)

if $\|\gamma^{l+1} - \gamma^l\| < \mathrm{tol}_\gamma$

$$PV^m = PV^{l+1}, \gamma^m = \gamma^{l+1}$$

$$m = m+1$$

$$z^{*m+1} = z^{*n} - \frac{\Delta t}{2}\left[\frac{\gamma^m}{2z_s^m} + \frac{\gamma^n}{2z_s^n} \right] + \frac{\Delta t}{2}\left[PV^m + PV^n \right]$$

if $\|z^{m+1} - z^m\| < \mathrm{tol}_z$
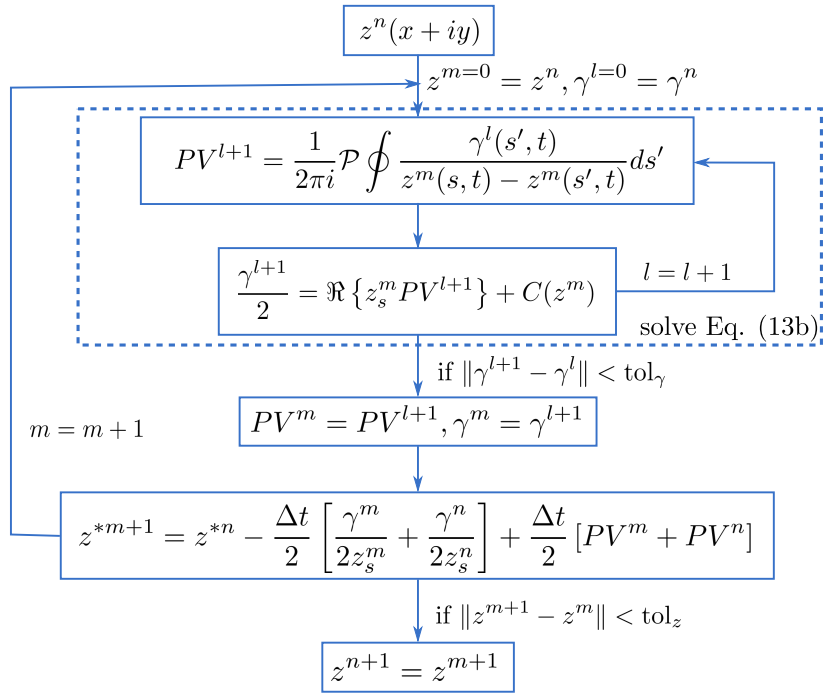
$$z^{n+1} = z^{m+1}$$

FIG. 6. Flow chart of the vortex-sheet algorithm using Crank–Nicolson for time advancement and fixed-point iteration for resolving the implicit nonlinear terms.
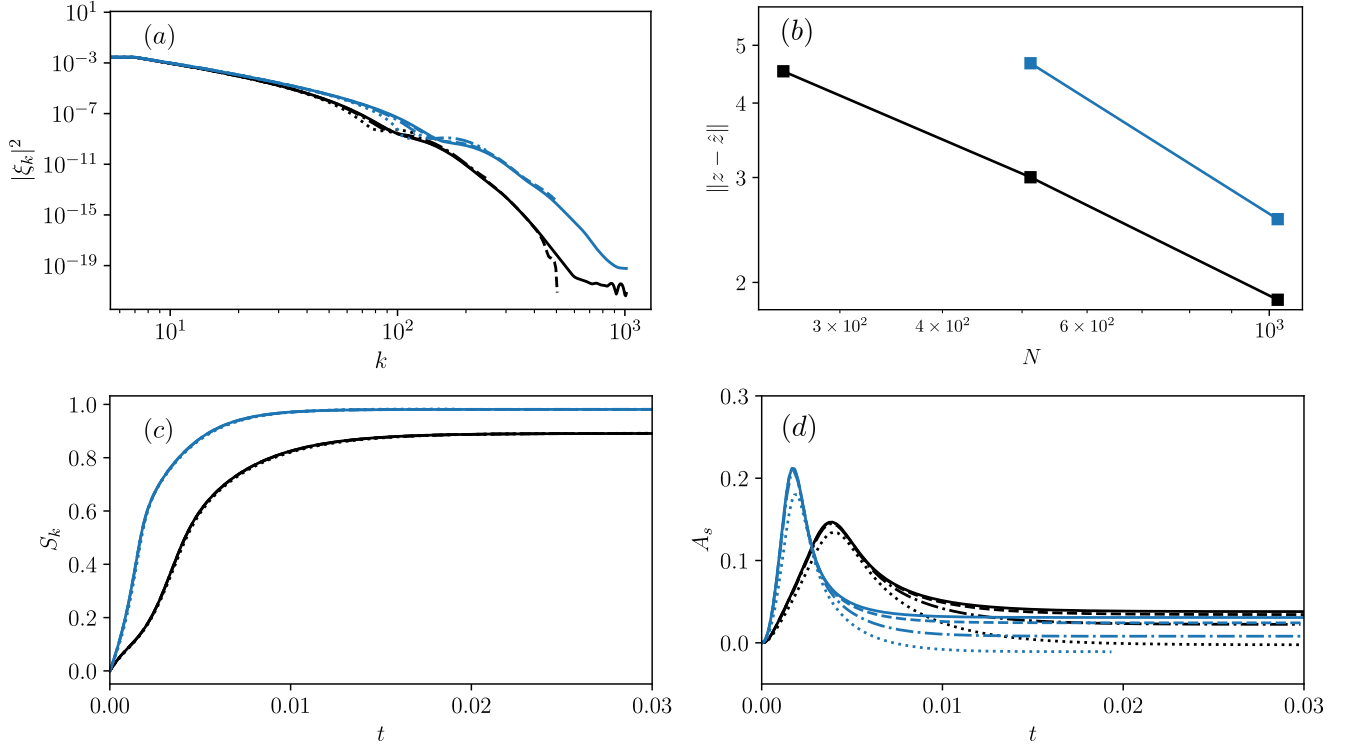

FIG. 7. Grid convergence study for fundamental modes $k_m = 7$ (black) and $k_m = 9$ (blue) with $\mathrm{N_{Ba}} = 1$ and $N = 256$ (dotted), $N = 512$ (dot-dashed), $N = 1024$ (dashed), and $N = 2048$ (solid). (a) Spectral energy of harmonic modes (k, $2k$, $3k$, ...). (b) The root-mean-square error taking the $N = 2048$ solution $\hat{z}$ as "exact". (c) Grid convergence of the evolution of the skewness $Sk(t)$. (d) Grid convergence of the evolution of the asymmetry $As(t)$.